Journal of the Korean Society for Nondestructive Testing
Vol. 27, No. 6 (2007. 12)

Visualization of Surface Deformation on an Open-Hole Specimen Based on Grating Shearography

Jung-Ryul Lee*,†, Seung Seok Lee** and Wonseok Chung***

Abstract This contribution contained the classical work of an open-hole tensile plate to demonstrate the performance of grating shearography and to compare with the results obtained by other full-field measurement techniques. The isotropic plate with an open-hole has often appeared in the previous contributions introducing novel full-field method and system. Grating shearography directly provided six quantitative measurands about the specimen's surface kinematics by using a single measurement set: three in-plane strains, in plane rotation, and two out-of-plane slopes. The quasi-plane wavefront of grating metrology led to high signal-to-noise ratio (SNR) and thus neither fitting nor filtering was applied, and the small shearing distance of 101 μm could be used. The small shearing distance provided the outstanding spatial resolution of 80 μm and sensitivity appropriate for experimental mechanics. Finally, the grating shearography enabled the visualization of the complex surface deformation around the hole and also detected parasitic flexions of the specimen in the micrometer regime during the tensile test.

Keywords: Grating Shearography, Mechanical Characterization, Open-Hole Specimen

1. Introduction

When a structure with a local geometrical irregularity, such as an oil hole, pinhole, keyway, or notch, is stressed, strain concentration occurs in the vicinity of the irregularity. The plate with a hole represents a classical structural problem and has been used in many industrial applications, particularly, in structural parts to be unable to avoid the hole despite design change. For instance, mechanical fastening through a bolt is commonly used to join structural members because of low cost, simplicity and ease of repair. For the experimental analysis of the hole-plate, electrical strain gages (ESGs) have been used since 1940s. They can be selectively applied to locations of interest. However, ESGs attached near such a strain concentration area (Kogo et al, 1998; Tan, 1994; Frocht and Hill, 1940; Regalbuto and Wheeler, 1970) average the strain over the gage area. Even if the recent ESGs can provide a high spatial resolution in millimeter regime in the forms of plural attachment of small size ESGs or electrical strain grid gage, it is insufficient to measure precisely the strain at distances close to the notch boundary where the maximum stress concentration is expected (Tan, 1994). In addition, although multi-axial ESGs operating on the same effective area exist, the measurands are limited to in-plane strains. We introduce here a three dimensional optical full-field method providing not only in-

Received: November 9, 2007, Accepted: December 21, 2007. * Department of Aerospace Engineering, Chonbuk National University, Jeonju, Chonbuk, 561-756, Korea, ** Nondestructive Evaluation Group, Korea Research Institute of Standards and Science, Daejon, 305-340, Korea, *** Railroad Structure Research Team, Korea Railroad Research Institute, 360-1, Woram-dong, Uiwang-city, Gyeonggi-do, 437-757, Korea, † Corresponding author: leejrr@chonbuk.ac.kr

plane strains but also local in-plane rotation and out-of-plane deformations directly as additional measurands. Indeed, whenever a novel full-field method is developed, open-hole tensile plates are used to determine the degree of improvement of the full-field method and system in terms of the spatial resolution (gage length) related to the approach measurement to the boundary of the hole or some notches and the number of extracted measurands. Strain concentration was measured by a variety of full-field measurement techniques such as caustics (Theocaris, 1973), transmission photoelasticity (Jessop et al, 1958; Lambert and Brailey, 1962), Moiré method (Theocaris, 1964; Post et al, 1994a), Moiré interferometry (Post et al, 1994b), speckle pattern interferometry (Hertwig et al, 1996; Ettemeyer, 1997; Lanza di Scalea et al, 1998). In the cases of Moiré interferometry and speckle pattern interferometry, surface deformation is mapped in terms of displacements or often mapped in terms of displacement contours in the case without phase-shifting technique. Lanza di Scalea et al. reported full-field strain results of a pin-load plate by fitting and differentiating the measured displacement maps. The spatial resolution in their experiment was about 0.4 mm (equivalent circle diameter=451 μm). Pandita et al. developed new photogrammetry for the full-field strain map. However, this was also an indirect strain measurement technique because the measurement principle was based on the displacement fields of the object points on the specimen surface. In the actual experiments, they lost the information close to the open hole to confirm a measurement area of 25×25 mm^2. Lagattu et al. applied the white light speckle correlation technique to a circular notched composite, and they obtained a high spatial resolution of 360×360 μm^2. equivalent to 406 μm for the displacement measurement. In fact, the calculation of the strain map from the displacement map is still a challenging part of displacement measurement techniques because of the rigid body motion associated with not the strain but the displacement and the need of a complex unwrapping technique. Moiré interferometry and speckle pattern interferometry are inherently susceptible to parasitic vibration, which obstructs exact measurement, and therefore, require special vibration isolation. For more practical applications, shearography technique is thus introduced in the classical interferometric techniques. Aebischer et al. used a direct strain measurement technique called image-shearing speckle pattern interferometry known now as speckle pattern shearography. The authors chose a large shearing distance of 5 mm to obtain enough sensitivity against speckle noise, and the measured phase fringe maps were all filtered to remove spatially distributed speckle noise. Therefore, the spatial resolution in their experiments was much more than 5 mm with respect to each shearing direction. Yang et al. presented six measurands of an open-hole tensile plate (material: Araldite B) based on speckle pattern shearography. Even if the shearing distance was not written clearly in their contribution, a small distance could be applied, but they did not test loading bearing engineering materials such as a composite or metal, which could generate sufficient fringes because of their relatively large deformation property despite the small shearing distance. However, the authors did not attach a quantitative strain indicator in their paper because of the difficulty of unwrapping caused by the collapsed fringe patterns and excessive fringe density. Here, it should be noted that the readers must distinguish speckle pattern shearography for quantitative mechanical characterization from one for nondestructive testing (Yoseph, 1999). The former is dealt in this paper.

This paper introduces grating shearography as a novel optical full-field measurement technique and it performances are demonstrated in an open-hole tensile plate. This classical and standard specimen enables to compare with those of other full-field measurement techniques.

Therefore, this contribution focus on demonstrating the merits of grating shearography such as direct strain measurement capability without filtering or fitting, multiple physical parameter measurement capabilities and wide controllable sensitivity, resolution and spatial resolution due to high SNR obtained by the diffraction grating.

2. Description of Grating Shearography

2.1 Optical Setup and Phase Determination

Figure 1 shows the optical setup for grating shearography. A collimated beam with a diameter of 150 mm obtained from 10-mW He-Ne laser illuminates the front surface of the specimen covered with a diffraction grating of 1200 lines/mm and the classical three-mirror setup (Post et al, 1994b). The manufacturing process of the specimen grating is shown in Fig. 2. The ready-to-bond diffraction gratings are mass-produced by the first and second steps and they are attached in the specimens based on epoxy. The actual thickness of the specimen grating made was 18 μm and thus the shear lag effect between the grating and the specimen was disregarded.

When we adjust the beam directions so that the zeroth order beams diffracted from the grating go back to the pinhole of the spatial filter assembled before the laser via the three-mirror setup, the four incidence angles become the same and this same angle can be calculated as follows.

$$\sin\theta = \frac{\lambda}{p_s} \tag{1}$$

where λ is the wavelength of laser, p_s is the pitch of the grating (p_s=10^6 nm/1200=833.3 nm) and θ denotes the common incidence angle of the four beams. Only one part of the whole circular divergent beam passes the screen located in front of lens1, **A**, **B**, **C** or **D** and then becomes collimated due to lens1. Therefore, the four illumination directions can be consecutively realized. The first order beam diffracted from the grating is focused by lens2, and then sheared in a modified Michelson interferometer. The Michelson interfermeter has a three-axis PZT actuated mirror capable of x-tilting, y-tilting and z-translation, which are controlled by a PZT -driver (Piezosystem Jena). Therefore, the

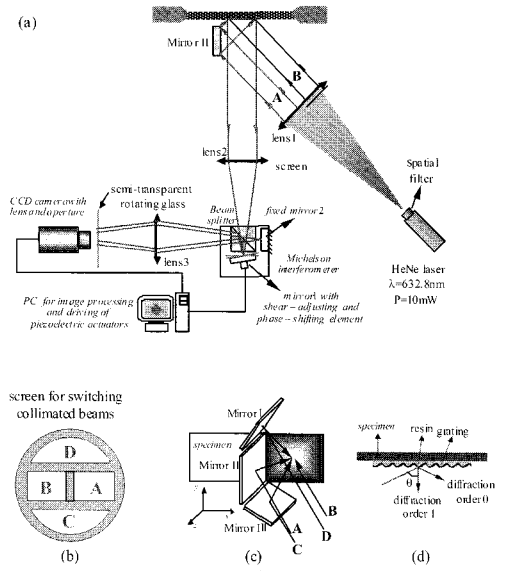

Fig. 1 Grating shearography system: (a) optical arrangement, (b) screen for switching the collimated beam, (c) three-mirror setup, (d) diffraction grating

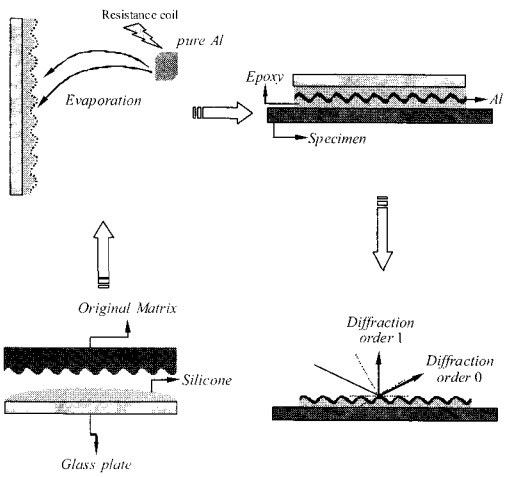

Fig. 2 Manufacturing process for diffraction grating and specimen grating

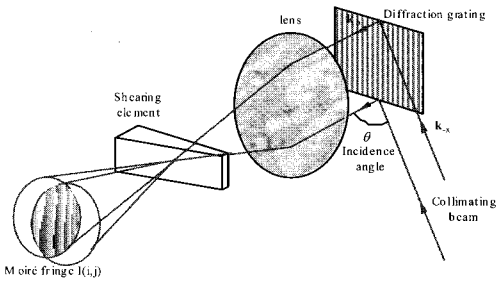

Fig. 3 Principle of fringe generation of grating shearography

shearing distance is adjusted in an open loop to the x(y)-direction by tilting about the y(x)-axis. The sheared beams generate a moiré fringe in the image plane, as explained in Fig. 3. In the real setup of Fig. 1, the images are observed on a rotating semi-transparent plate for optical spatial filtering, which removes speckle noise. A CCD camera equipped with a lens system is used to take images. The CCD camera is connected to an image acquisition board plugged in a personal computer. The software Frangyne® developed at INM (Institut National de Métrologie, Techlab company) is installed to control the shearing distance and direction and the phase-shifting elements. It is also used for the data acquisition, the phase calculation, and the post processing of the acquired images.

A temporal phase-shifting algorithm is used for the quantitative phase determination of the acquired intensity field with a moiré fringe pattern. The intensity field can be rearranged as follows.

$$I(i,j) = < I > [1 + m\cos(\phi)] \tag{2}$$

where $<I>$ is the average intensity, $m(i,j)$ is the contrast, and $\phi(i,j)$ is the phase map in each step. The windowed discrete Fourier transform (WDFT) algorithm is used for phase determination (Surrel and Fournier 1999). The amount of phase shift is $\pi/2$, and one set is composed of seven phase-shifted intensity samples. The resulting form with a triangular window is represented as follows.

$$\tan\phi = \frac{(I_0 - I_6) - 3(I_2 - I_4)}{2(I_1 + I_5) - 4I_3} \tag{3}$$

where I with the subscripts imply consecutively phase-shifted intensity maps.

2.2 Relations between the Determined Phases and Displacement Derivatives

In Fig. 4a, we consider the light paths from the outlet of the laser source to the image plane via the points $P(i,j)$ and $P_s(i,j)$, which are imaged onto a single point in the image plane by means of the shearing device. In the initial state of the object, the phase difference resulting from the unequal path lengths as shown in Fig. 4a is

$$\phi^r = (\mathbf{k}_o - \mathbf{k}_x) \cdot \mathbf{\Delta}_x \tag{4}$$

where Δ_x is the shear vector. $\mathbf{k}_x$ and $\mathbf{k}_o$ are the illumination and observation vectors, respectively.

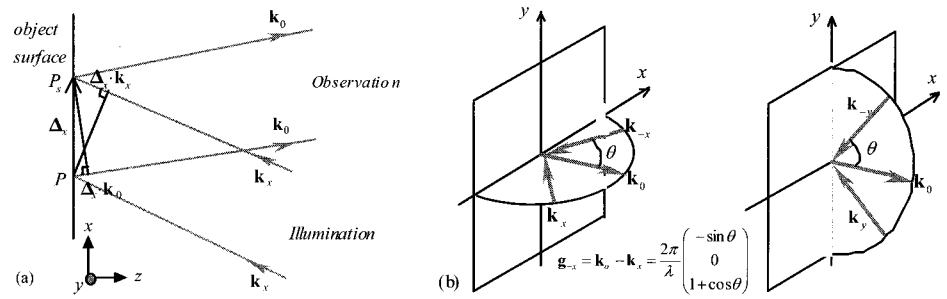

Fig. 4 (a) Geometry of object surface, (b) illumination, observation and sensitivity vectors

Because of the deformation of the object, point P is displaced to P' (displacement vector **d**(P)), and P_s to P_s' (displacement vector **d**(P_s)). The vector between these displaced points is

$$\boldsymbol{\Delta}_x^{'} = \boldsymbol{\Delta}_x + \mathbf{d}(P_s) - \mathbf{d}(P) \tag{5}$$

and the phase difference in the deformed state is

$$\phi^d = (\mathbf{k}_o - \mathbf{k}_x)\cdot\boldsymbol{\Delta}_x^{'} = (\mathbf{k}_o - \mathbf{k}_x)\cdot[\boldsymbol{\Delta}_x + \mathbf{d}(P_s) - \mathbf{d}(P)] \tag{6}$$

The phase change resulting from the deformation of the object is calculated by subtracting the phase difference of the reference state from that of the deformed state.

$$\Delta\phi = \phi^d - \phi^r = (\mathbf{k}_o - \mathbf{k}_x)\cdot[\mathbf{d}(P_s) - \mathbf{d}(P)] \tag{7}$$

We next define the sensitivity vector and the displacement difference as follows (see Fig. 4b).

$$\mathbf{g} = \mathbf{k}_o - \mathbf{k}_x \tag{8}$$

$$\Delta\mathbf{d} = \mathbf{d}(P_s) - \mathbf{d}(P) \tag{9}$$

The term $\Delta\mathbf{d}$ can be developed into a Taylor series in the shearing distance $\Delta_x = |\,\Delta_x\,|$, which results in

$$\Delta\mathbf{d} = \frac{\partial\mathbf{d}}{\partial x}\Delta_x + \frac{1}{2}\frac{\partial^2\mathbf{d}}{\partial x^2}\Delta_x^2 + \frac{1}{6}\frac{\partial^3\mathbf{d}}{\partial x^3}\Delta_x^3 + \cdots\cdots \tag{10}$$

By neglecting the higher-order terms of the Taylor series, we obtain

$$\Delta\phi = \mathbf{g}\cdot\frac{\partial\mathbf{d}}{\partial x}\Delta_x \tag{11}$$

where $\Delta\mathbf{d}=[u\ v\ w]$ is the displacement vector at P. Eqn. (11) shows that three parts contribute to the phase change measured by shearography. The deformations of the object appear in the form of the derivatives in the shearing direction of the displacement vector $\Delta\mathbf{d}$. The directions of illumination and observation and the laser wavelength determine the sensitivity vector **g**. The third contribution is the shearing distance Δ_x.

2.3 Isolation of Measurands

Due to the classical three-mirror arrangement, the object surface is consecutively illuminated by the four beams with wave vectors, $\mathbf{k}_x$, $\mathbf{k}_{-x}$, $\mathbf{k}_y$, $\mathbf{k}_{-y}$, as shown in Fig. 4b. For each illumination, a shearing distance (Δ_x or Δ_y) is realized, horizontally or vertically, and the phase of the moiré fringe pattern is obtained by a phase-shifting technique at each time, which is realized by the piston movement of the PZT-actuated mirror in the Michelson interferometer. Therefore, eight phase change maps ($\Delta_{x,x}=\phi^d_{x,x} - \phi^r_{x,x}$, $\Delta\phi_{-x,x}$, $\Delta\phi_{y,x}$, $\Delta\phi_{-y,x}$, $\Delta\phi_{x,y}$, $\Delta\phi_{-x,y}$, $\Delta\phi_{y,y}$ and $\Delta\phi_{-y,y}$) for one loading step are calculated from two sets composed of eight phase maps, where the first indices represent the directions of the sensitivity vectors and the second ones indicate the shearing directions. The exponent *d* or *r* means a deformed state or reference state. Then the following sensitivity vectors are obtained (see Fig. 4b).

$$\mathbf{g}_x = \frac{2\pi}{\lambda}\begin{pmatrix}\sin\theta\\0\\1+\cos\theta\end{pmatrix},\ \mathbf{g}_{-x} = \frac{2\pi}{\lambda}\begin{pmatrix}-\sin\theta\\0\\1+\cos\theta\end{pmatrix},$$
$$\mathbf{g}_y = \frac{2\pi}{\lambda}\begin{pmatrix}0\\\sin\theta\\1+\cos\theta\end{pmatrix},\ \mathbf{g}_{-y} = \frac{2\pi}{\lambda}\begin{pmatrix}0\\-\sin\theta\\1+\cos\theta\end{pmatrix} \tag{12}$$

And the differential displacement vector components for the two shearing distances Δ_x and Δ_y are

$$\Delta\mathbf{d}_x = \frac{\partial\mathbf{d}}{\partial x}\Delta_x = \begin{pmatrix}\partial u/\partial x\\\partial v/\partial x\\\partial w/\partial x\end{pmatrix}\Delta_x$$
$$\Delta\mathbf{d}_y = \frac{\partial\mathbf{d}}{\partial y}\Delta_y = \begin{pmatrix}\partial u/\partial y\\\partial v/\partial y\\\partial w/\partial y\end{pmatrix}\Delta_y \tag{13}$$

Denoted $\Delta=\Delta_x=\Delta_y$, $C_1=(2\pi/\lambda)\Delta\sin\theta$, and $C_2=(2\pi/\lambda)\Delta(1+\cos\theta)$, the eight phase change maps can be represented by the following equations.

$$\Delta\phi_{x,x} = C_1\frac{\partial u}{\partial x} + C_2\frac{\partial w}{\partial x},\ \Delta\phi_{-x,x} = -C_1\frac{\partial u}{\partial x} + C_2\frac{\partial w}{\partial x}$$
$$\Delta\phi_{y,x} = C_1\frac{\partial v}{\partial x} + C_2\frac{\partial w}{\partial x},\ \Delta\phi_{-y,x} = -C_1\frac{\partial v}{\partial x} + C_2\frac{\partial w}{\partial x}$$
$$\Delta\phi_{x,y} = C_1\frac{\partial u}{\partial y} + C_2\frac{\partial w}{\partial y},\ \Delta\phi_{-x,y} = -C_1\frac{\partial u}{\partial y} + C_2\frac{\partial w}{\partial y}$$
$$\Delta\phi_{y,y} = C_1\frac{\partial v}{\partial y} + C_2\frac{\partial w}{\partial y},\ \Delta\phi_{-y,y} = -C_1\frac{\partial v}{\partial y} + C_2\frac{\partial w}{\partial y} \quad (14)$$

These equations can be used to calculate the displacement derivative components.

$$\frac{\partial u}{\partial x} = (\Delta\phi_{x,x} - \Delta\phi_{-x,x})/2C_1 = \varepsilon_{xx},$$
$$\frac{\partial v}{\partial y} = (\Delta\phi_{y,y} - \Delta\phi_{-y,y})/2C_1 = \varepsilon_{yy} \quad (15)$$

$$\frac{\partial u}{\partial y} = (\Delta\phi_{x,y} - \Delta\phi_{-x,y})/2C_1,$$
$$\frac{\partial v}{\partial x} = (\Delta\phi_{y,x} - \Delta\phi_{-y,x})/2C_1 \quad (16)$$

$$\frac{\partial w}{\partial x} = (\Delta\phi_{x,x} + \Delta\phi_{-x,x})/2C_2 = (\Delta\phi_{y,x} + \Delta\phi_{-y,x})/2C_2 \quad (17)$$

$$\frac{\partial w}{\partial y} = (\Delta\phi_{x,y} + \Delta\phi_{-x,y})/2C_2 = (\Delta\phi_{y,y} + \Delta\phi_{-y,y})/2C_2 \quad (18)$$

The digitalized phase change maps were cut to be matrices with the same number of pixels. The phase subtraction or addition between the two dimensional digitalized phase change maps was done by pixel by pixel, which results in subtracted or added phase maps. As shown in eqns. (15) through (18), the four measurands are directly isolated from the measured phase change maps. In particular, the x-slope and the y-slope, which are the two partial derivatives of the out-of-plane displacement of eqns. (17) and (18), can be measured independently in two different ways. This is due to the use of four illuminations instead of three illuminations (Walner and Brem, 1999), the minimum number of illuminations (six equations for six unknowns). Additional two measurands can be derived by using the set of $\partial u / \partial y$ and $\partial v / \partial x$ in eqn. (16). One of them is the shear strain (ε_{xy}) and the other is the local in-plane rotation (ω_z), as shown in the following equations.

$$\varepsilon_{xy} = \frac{1}{2}\left(\frac{\partial u}{\partial y} + \frac{\partial v}{\partial x}\right),\quad \omega_z = \frac{1}{2}\left(\frac{\partial v}{\partial x} - \frac{\partial u}{\partial y}\right) \quad (19)$$

Consequently, grating shearography with four illuminations provides six measurands by a single measurement set.

3. Experiments

The test object was a tensile specimen with a length of 85 mm, width of 10 mm and thickness of 1.47 mm, containing a central hole of 3 mm in diameter. The plate is made of Al-alloy having E=70 GPa and ν=0.33. A grating was bonded on the front surface of the specimen after drilling the Al-alloy specimen. In general, drilling damages around the grating part at the hole boundary occur in the general process of drilling after bonding. During the bonding, we made a cavity in the support under the specimen so that the resin may not refill the hole. By doing so, we could avoid the drilling damage of the hole boundary simply by making the cavity an exit of surplus resin. The surface deformation of the specimen induced by an external load was digitized in the form of phase according to deformation of this grating. The tabletop tensile tester and the dimensions and loading condition of the specimen are presented in Fig. 5.

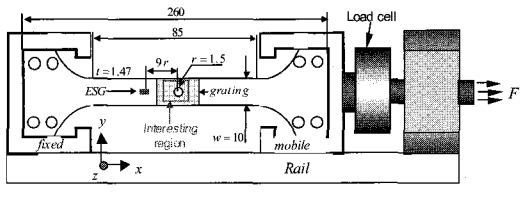

Fig. 5 Tabletop tensile tester, the geometry and loading condition of the specimen [in mm].

The region of interest in this experiment was an area of 9.74×7.76 mm^2 including the hole, which corresponded to 184×135 $pixel^2$. A displacement was imposed on the movable jaw. The load was controlled by using a classical load cell, and an ESG bonded beside the grating was used for the comparison of the experimental results with the results of grating shearography. The specimen was loaded in the four steps, 209 N, 436 N, 599 N and 813 N. At each load step, eight phase maps were determined by the combination between four directional illuminations and two directional shearings. Seven intensity maps obtained by the phase-shifting device calculated one phase map of eight combinations. Subsequently, eight phase change maps were calculated by the software Frangyne® for each combination between two different load steps. The SNR of a typical phase map ($\Delta\phi_{-x,x}$) defined in $10\log_{10}$(signal variance/noise variance), was 16.01 dB at 812N step. Six measurands were next analyzed at each measurement step in the same software by using the illumination angle of 49.41°, the laser wavelength of 632.8 nm, and the applied shearing distance ($\Delta=\Delta_x=\Delta_y$). The shearing distance is a function of the relative angle between the two mirrors inside the Michelson interferometer. The shearing distance in each direction was 101 μm in this experiment which was measured by spatial phase -shifting grid method (Surrel and Fournier, 1996). The phase variation of 2π corresponded to 4165 με (2083 με / 2083 μrad / 1914 μrad) for normal and transverse strain measurements (shear strain / local in-plane rotation / slope measurements). In these calculations, neither fitting nor filtering methods were used. In the end, two strain maps in eqn. (15) and two slope maps in eqns. (17) and (18) dependent on the single directional shearing distance had a spatial resolution of 84 μm, and the shear strain and the local rotation maps in eqn. (19) related to both directional shearing distances had a special resolution of 101 μm. As for the resolution, the standard deviations of temporal phase noises ($\sigma_{\Delta\phi_{x,x}}=\sigma_{\phi^{t2}_{x,x}-\phi^{t1}_{x,x}}/\sqrt{2}$, $\sigma_{\Delta\phi_{-x,x}}$, $\sigma_{\Delta\phi_{y,x}}$, $\sigma_{\Delta\phi_{-y,x}}$, $\sigma_{\Delta\phi_{x,y}}$, $\sigma_{\Delta\phi_{y,y}}$) were determined by the repeatability measurements. From these values, the resolutions of the six measurands can be determined (Lee, 2005). The tensile strain (transverse strain / shear strain / local in-plane rotation / x-slope / y-slope) maps had a resolution of 30.08 με (40.16 με / 25.74 με / 25.74 μrad / 19.57 μrad / 20.01 μrad). These spatial resolution and resolution can be easily controlled by Gaussian least square filtering, which improves the resolution but degrades the spatial resolution. Therefore, the interdependent performances can be suitably adjusted according to the degree of heterogeneity of the object surface. However, if the filtering process is a prerequisite as in speckle pattern interferometry and shearography, the tradeoff controllable range between the resolution and the spatial resolution will be considerably reduced.

4. Results and Discussion

The hole influence on the strain distribution shows up on the four full field maps, as shown in Fig. 6. High strain values were immediately concentrated at the top and bottom of the hole, whereas the zones in the left and right of the

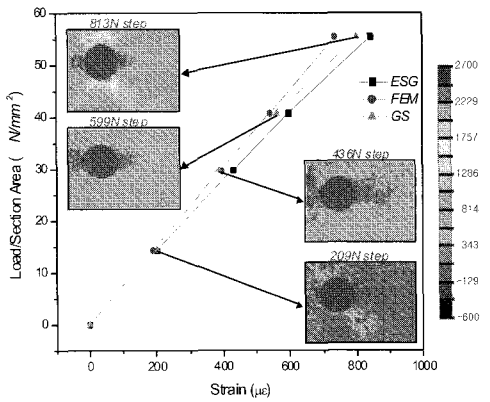

Fig. 6 Full-field tensile strain distributions in each loading step during the tensile test (GS: grating shearography)

hole were relieved from stress. Therefore, the strain in the left and right zones tended to approach zero at closer distances to the hole. Three stress-strain curves in Fig. 6 were obtained by a 1×1 mm^2-ESG at the distance of $9r$ and by grating shearography and finite element method (FEM) at the distance of $4.26r$ from the center of hole. At this time, the results of grating shearography were averaged in the same virtual area as the effective area of the ESG. The experimental and numerical plots showed good agreement. Fig. 7a shows that the strain relief region at both sides of the hole was relatively deepened with the increase of the tensile load. Fig. 7b shows the strain concentration at the top and bottom of the hole, on the net section perpendicular to the loading axis, versus the distance from the hole. FEM and grating shearography showed good agreement as well in this graph. For these graphs, Gaussian least-square filtering with a 7×7 $pixel^2$ kernel was applied for these strain profiles to improve the SNR, but it was not applied for the full-field strain maps.

Figure 8 shows the full-field strain comparison result between grating shearography and FEM for each in-plane strain component (ε_{xx}, ε_{yy} or ε_{xy}). The general trend between the experimental and numerical maps showed excellent correlation. As an interesting physical parameter, the grating shearography provided the local in-plane rotation map at each loading step as presented in Fig. 9, where the X-shaped local in-plane rotation distribution in the circumference of the hole and its line profiles explained the deformation mechanism in which the hole became slightly elliptical due to the tensile loading.

The grating shearography also provided out-of-plane information separated into two partial differential terms ($\partial w(x, y) / \partial x$ and $\partial w(x, y) / \partial y$). Fig. 10 presents the x-slope and y-slope maps during the tensile test, respectively. As shown in the line profiles, there was considerable x-directional parasitic flexion, globally. Quantitatively, the maximum out-of-plane displacement was 33.08 μm, and it corresponded to 3.388 μm per 1 mm. As for the

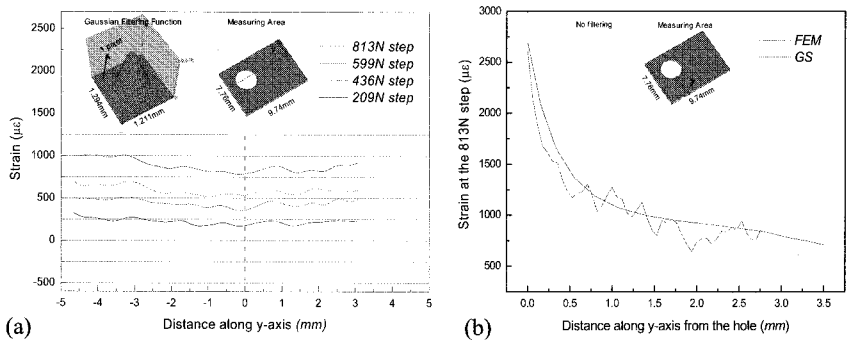

Fig. 7 Line profiles of the tensile strain (a) on the net section at the distance of 3.263r from the hole (b) on the net section along the centerline of the hole perpendicular to the loading axis

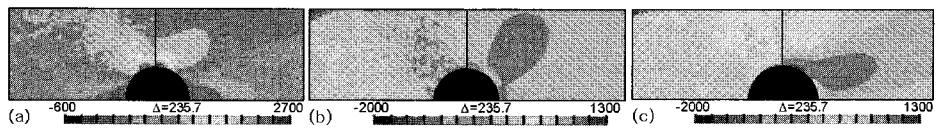

Fig. 8 (a) tensile, (b) transverse, and (c) shear strain maps at 813N step: experiment(left) and FEM(right) (in microstrain)

y-directional parasitic flexion, the maximum out-of-plane displacement was –6.36 μm, which corresponded to –0.820 μm per 1 mm. Consequently, the x-directional parasitic flexion was 4.13 times as much as the y-directional parasitic flexion. The x-directional parasitic flexion was due to the misalignment between the fixed and movable jaws of the tabletop tensile tester in Fig. 5. On the contrary, these results demonstrate that grating shearography had sufficient sensitivity to detect the defects of the test fixtures, although the system sensitivity was reduced by the use of the small shearing distance. Consequently, grating shearography can be used to modify and optimize test devices and fixtures and to develop the specimen standard. In this experiment, the sensitivity (s) for the slope maps is

$$s_{slopes}(\lambda,\theta,\Delta)=\frac{\partial\phi}{\partial M}= \left(\frac{4\pi}{\lambda}\right)(1+\cos\theta)\Delta=0.18781^\circ/\mu rad \tag{20}$$

where M is the measurand. Shearography has one additional parameter for controlling system sensitivity than classical interferometry: the

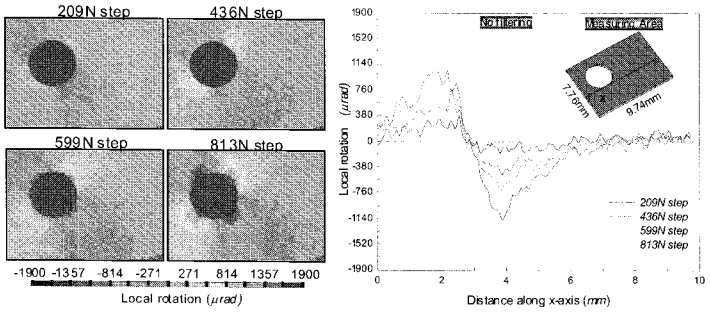

Fig. 9 In-plane local rotation maps and line profiles in each step

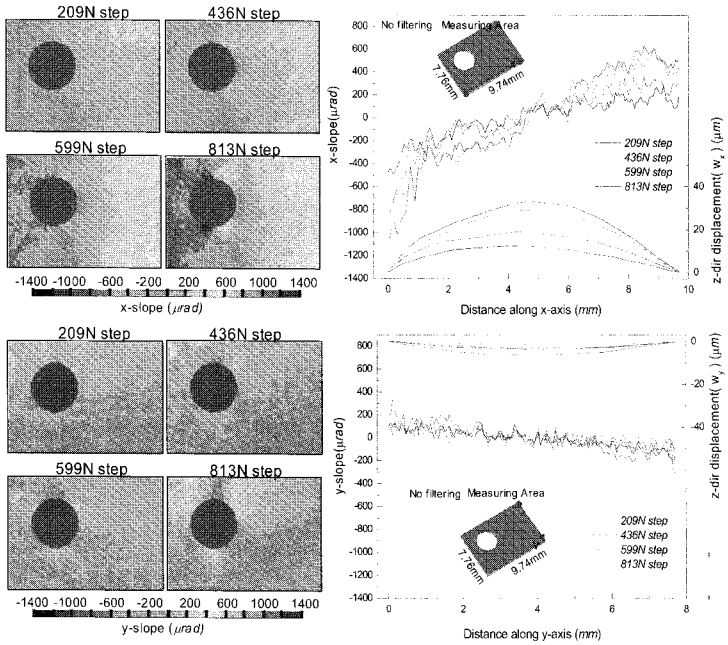

Fig. 10. X-slope and y-slope maps, line profiles and z-displacements along x-and y-axis in each step

shearing distance, as described in eqn. (20). Actually, the wavelength of the laser and the incidence angle of the laser beam cannot be controlled easily in a given optical setup. These are issues in the step of system design. On the other hand, shearing distance can be controlled depending on the experimental requirements. In other words, a larger shearing distance can be used for experimental conditions requiring high sensitivity.

However, a large shearing distance can be used at the expense of degradation of spatial resolution. The small shearing distance such as 101 μm was used in this experiment because of the good SNR due to the quasi-plane wavefront obtained from the diffraction grating.

For nondestructive testing application, the deformation near damage is generally great in comparison with the intact case. And even when we use thermal load or mechanical load that is usually for out-of-plane deformation, the damaged area is deformed easily enough to detect the damage. Therefore, it is not necessary to use a large shearing distance. In other words, the degree of the deformation is high and thus SNR is high even in a small shearing distance. Also, if the target material is not a load-bearing material such as epoxy, plastics, tire and so on, deformation is relatively greater than that in the load-bearing material in a given load. In this case, it is not necessary either to use a large shearing distance. However, for mechanical characterization application under the scheme of nondestructive evaluation, the target specimen is usually intact and the strain gradient, material heterogeneity and so on are visualized. In addition, if the material is a load-bearing material such as al-alloy, steel, reinforced plastics, it is difficult to obtain sufficient sensitivity by using a small shearing distance in micrometer regime, especially for in-plane strains. Therefore, speckle pattern shearography applied for mechanical characterization has selected a large shearing distance in millimeter regime.

The parasitic global flexions discussed above could be numerically removed by tilting the out-of-plane displacement derivative maps. The local x(y)-slope maps in which the x(y)-directional global flexion of the specimen has been eliminated are shown in Fig. 11. We can ascertain from the information on out-of-plane displacements (w_x and w_y) separated into x and y directions that the thickness at the top and bottom of the hole decreased sharply and the thickness of the zones in the left and right of the hole increased at closer distances to the hole boundary. The former was due to the strain concentration at the top and bottom of the hole and the latter was due to the strain relief on both sides of the hole.

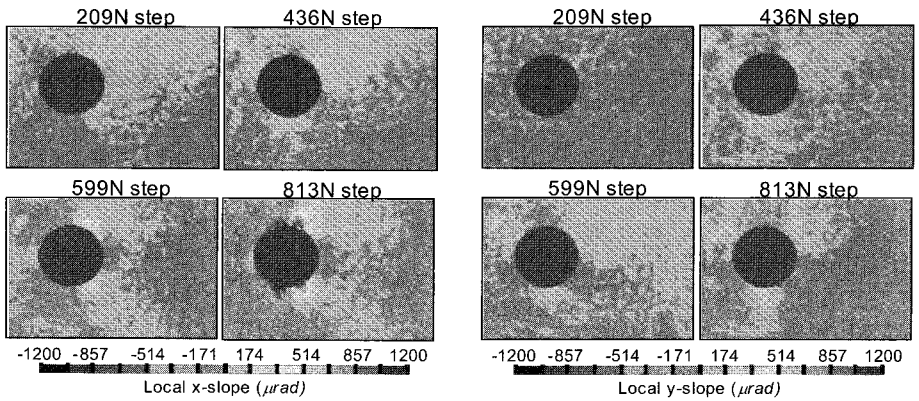

Fig. 11 Local x-slope and y-slope maps in each step (the global parasitic flexions of the specimen were eliminated)

5. Conclusions

Grating shearography was used to measure the in-plane strain and local rotation fields and the x-and y-slope fields of the open-hole tensile plate, directly. The several merits of this full-field surface deformation visualization method were demonstrated through the classical mechanical problem.

1. Direct strain measurement technique with neither filtering nor fitting

Many optical methods measure displacement. The numerical differentiation of a noisy displacement map for a strain map is still a challenging part of displacement measurement techniques. To overcome this drawback, we used optical differentiation; the strains could be directly isolated because the strains are functions of displacement derivatives. The quasi-plane wavefront obtained by the artificial grating and the optical spatial filtering to remove speckle noise yielded good SNR of raw images. Neither numerical filtering nor fitting was thus necessary.

2. One measurement set and six measurands

Grating shearography with the four sensitivity vector directions provided six quantitative measurands about the surface kinematics of a specimen by using one measurement set: three in -plane strains, in-plane rotation and two out-of-plane slopes. The in-plane strains were verified by FEM. The others enabled the visualization of the deformed shape of the specimen and the comprehensive understanding of the strain fields. Also, grating shearography showed excellent performance for the detection of the parasitic flexion of the tensile tester used in this experiment. These results imply that grating shearography can be used as an apparatus to improve and optimize test devices and fixtures and to develop a standard specimen.

3. Wide controllable sensitivity, resolution and spatial resolution

The excellent SNR of the grating shearography allowed a wide controllable range of sensitivity. In fact, the oversensitivity of the classical interferometry has raised problems in post-image processing and in environment with vibration and rigid body motion. Speckle pattern shearography has needed a large shearing distance for sufficient sensitivity, but a large shearing distance raises problems in mechanical characterization such as missing data around material discontinuity and degradation of spatial resolution. Grating shearography solved both problems of oversensitivity based on shearography technique and low sensitivity at a small shearing distance by improving SNR through the use of diffraction grating. The shearing distance was an additional controllable parameter of shearography, which was not controllable in classical interferometry. It is a very useful controllable parameter for determining the system sensitivity according to experimental requirements. Due to the small shearing distance and the good SNR, the low-pass filtering was not essential and hence spatial resolution did not show degradation associated with filtering. On the other hand, if a measurement is subjected to speckle noise as in speckle pattern shearography, the shearing distance should be increased to guarantee the insensitivity of quantitative measurement to the level of the noise. Moreover, the high SNR led to a high resolution even though low-pass filtering was not used. Therefore, three interdependent performances could be suitably adjusted in a wider range.

Acknowledgement

This work was supported by the Korea Science and Engineering Foundation (KOSEF) grant funded by the Korea government (MOST) (No. 2007-00467). The authors would also like to acknowledge the useful advice of Prof. Alain Vautrin and his research team.

References

Aebischer, H. A. and Waldner, S. (1997) Strain Distributions Made Visible with Image-Shearing Speckle Pattern Interferometry, Optics and Lasers in Engineering, Vol. 26, 407-420

Ettemeyer, A. (1997) *Miniaturized 3D-ESPI-Sensor for Material Testing*, SEM, Washington, USA.

Frocht, M. M. and Hill, H. N. (1940) Stress-Concentration Factors around a Central Circular Hole in a Plate Loaded Pin in the Hole, Journal of Applied Mechanics, Vol. 1, pp. 5-9

Hertwig, M., Flemming, T., Flourux, T. and Aebischer, H. A. (1996) Speckle Interferometric Damage Investigation of Fibre-Reinforced Composites, Optics and Lasers in Engineering, Vol. 24, pp. 485-504

Jessop, H. T., Snell, C. and Holister, G. S. (1958) Photoelastic Investigation on Plates with Single Interference-Fit Pins with Load Applied (a) to Pin Only and (b) to Pin and Plate Simultaneously, The Aeronautical Quarterly, May, pp. 147-163

Kogo, Y. Hatta, H., Kawada, H. and Machida, T. (1998) Effect of Stress Concentration on Tensile Fracture Behaviour of Carbon-Carbon Composites, Journal of Composite Materials, Vol. 32, pp. 1273-1294

Lagattu, F., Lam, T. Q., Brillaud, J. and Lafarie-Frenot, M. C. (2002) White Light Speckle Correlation Applied to Strain Measurement in Notched Composites, ECCM10, Brugge, Belgium

Lambert, T. H. and Brailey, R. J. (1962) The Influence of the Coefficient of Friction on the Elastic Stress Concentration Factor for a Pin-Jointed Connection, The Aeronautical Quarterly, Feb, pp. 17-29

Lanza di Scalea, F., Hong, S. S. and Cloud, G. L. (1998) Whole-Field Strain Measurement in a Pin-Loaded Plate by Electronic Speckle Pattern Interferometry and the Finite Element Method, Experimental Mechanics, Vol. 38, No. 1, pp. 55-60

Lee, J. R. (2005) Spatial Resolution and Resolution in Phase-Shifting Laser Interferometry, Measurement Science and Technology, Vol. 26, pp. 2525-2533

Pandita, S. D., Huysmans, G., Verpoest, I. and Nishiyabu, K. (2000) Strain Fields around a Hole or a Crack in Woven Fabric Composites under On-Axis and Off-Axis Tensile Loading, ECCM9, Brighton, UK

Post, D., Han, B. and Ifju, P. (1994a) *High Sensitivity Moiré: Projection Moiré*, Springer Verlag, New-York, USA, pp. 124-130.

Post, D., Han, B. and Ifju, P. (1994b) *High Sensitivity Moiré: Moiré interferometry*, Springer Verlag, New-York, USA, pp. 135-226.

Regalbuto, J. A. and Wheeler, O. E. (1970) Stress Distributions from Interference Fits and Uniaxial Tension, Experimental Mechanics, Vol. 10, No. 7, pp. 274-280

Surrel, Y. and Fournier, N. (1996) Displacement Field Measurement in the Nanometer Range, in C. Gorecki (Eds.), *Optical Inspection and Micromeasurements*, SPIE 2782, Besancon, France, pp. 233-242

Surrel, Y. (1999) *Photomechanics-Fringe Analysis*, Springer Verlag, pp. 55-102

Tan, S. C. (1994) *Stress Concentrations in Laminated Composites*, Technomic, New York, USA

Theocaris, P. S. (1964) Isopachic Patterns by the Moiré Method, Experimental Mechanics, Vol. 4, pp. 153-159

Theocaris, P. S. (1973) Optical Stress Rosette Based on Caustics, Applied Optics, Vol. 12, pp. 380-387

Waldner, S. and Brem, S. (1999) Compact Shearography System for the Measurement of 3D Deformation, SPIE3745, pp. 141-148

Yang, L. X., et al. (1995) Precision Measurement and Nondestructive Testing by Means of Digital Phase Shifting Speckle Pattern and Speckle Pattern Shearing Interferometry, Measurement, Vol. 16, pp. 149-60

Yoseph, B. (1999) In-Service NDE of Aerospace Structures – Emerging Technologies and Challenges at the End of the 2nd Millennium, NDT.net, Vol. 4, No. 9